

Wave analysis of Airy beams and Airy Pulsed Beams

Yan Kaganovsky[†] and Ehud Heyman[‡]

[†]*Duke University, Dept. of Electrical and Computer Engineering,
Durham, NC 27708, USA, e-mail: yankagan@gmail.com*

[‡]*Tel Aviv University, School of Electrical Engineering,
Tel Aviv 69978, Israel*

Abstract

The Airy beam (AiB) has attracted a lot of attention recently because of its intriguing features. We have previously provided a cogent physical explanation for these properties by showing that the AiB is, in fact, a caustic of rays that radiate from the tail of the Airy function aperture distribution. We have also introduced a class of ultra wide band (UWB) Airy pulsed beams (AiPB), where a key step has been the use of a proper frequency scaling of the initial aperture field that ensures that all the frequency components propagate along the same curved trajectory so that the wavepacket of the AiPB does not disperse. An exact closed form solution for the AiPB has been derived using the spectral theory of transients (STT) which is an extension of the well know Cagniard–de Hoop (CdH) method. In this paper we discuss the properties of the AiB and AiPB, and use the present problem to discuss the relation between the CdH method and the STT.

1 Introduction

Recently, a class of Airy beam (AiB) solutions of the paraxial time-harmonic wave equation was introduced [1–4]. Originally, these beams were formulated in a 2D coordinate space, say (x, z) , and were generated by setting an Airy function as the initial field distribution in the aperture plane $z = 0$. Later on, finite energy AiB's were obtained by multiplying the Airy function aperture distribution by exponential or Gaussian windows, leading to closed form field solutions in [2] and [3], respectively.

Pulsed Electromagnetic Fields: Their Potentialities, Computation and Evaluation
I. E. Lager and L. J. Jiang (Eds.). © 2013 Delft University of Technology and IOS Press.
All rights reserved.

This article is published online with Open Access by IOS Press and distributed under the terms of the Creative Commons Attribution Non-Commercial License.
doi: 10.3233/978-1-61499-230-1-1

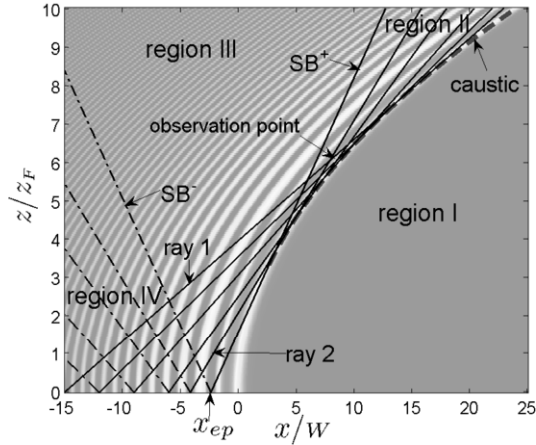


Figure 1: Ray description of the Airy beam plotted on a background of the intensity of the Airy beam in (2) (see [6, Fig. 1]). The z and x axes are normalized with respect to the Fresnel length z_F and the beamwidth W , respectively. As discussed in (7), the rays of species \hat{U}^+ (solid lines) radiate to the right with respect to the z -axis and converge to a caustic that delineates the AiB propagation trajectory. Species \hat{U}^- (dashed-dotted lines) radiates to the left and diverges. As discussed in (8), species \hat{U}^+ has additional set of rays that emerge from distant points in the aperture (beyond the figure frame) and do not converge on that caustic. These rays are shown in Fig. 2 but they have been removed here for clarity. Other parameters that appear in this figures are used in [6] but are not used here.

The AiB's attracted a lot of attention because of their intriguing features, the most distinctive one is the propagation along *curved* trajectories in free-space. These beams are also weakly diffractive along their trajectories, i.e., they retain their structure and remain essentially diffraction-free for distances that are much longer than the conventional diffraction (Rayleigh) length of Gaussian beams with the same width [2]. Another interesting feature, pointed out in [5], is the ability of the AiB to 'heal' itself, i.e., regenerate itself if the main beam is obstructed.

A cogent physical description to the AiB's and their intriguing properties has been presented in [6]. In that paper we have shown that the AiB is not generated by the main lobe of the Airy function in the aperture, but rather it is a caustic of rays that emanate from the oscillatory tail of this function and then focus on the caustic (Fig. 2). This also implies that the evolution of the main lobe of the AiB along the curved trajectory is not described by a local wave dynamics, and hence it cannot be regarded as a 'beam field' in that sense. These concepts were extended in [7] to construct an AiB

in a 3D coordinate space, where the structure of the caustic is much more complicated and requires the use of catastrophe theory.

The results of [6] have been utilized in [8] to introduce a class of ultra wide band (UWB) Airy pulsed beams (AiPB) with *frequency independent* ray skeleton, thus ensuring that all the frequency components of the AiB propagate along the same curved trajectory and in the overall, the AiPB wavepacket does not disperse. We also derived an exact closed-form TD solution for the AiPB via the spectral theory of transients (STT) [9–12]. The TD properties of the AiPB provide further insight into the wave mechanism of the AiB. Finally, in [7] we extended the non dispersive AiB solution to a 3D space where the caustic has the much more complicated structure of a *hyperbolic umbilic* catastrophe that evolves into a *parabolic umbilic* catastrophe.

The STT is an extension of the celebrated Cagniard–de Hoop (CdH) method [13–15] for the direct inversion into the TD of FD solutions that are given as spatial-spectrum integrals. In the CdH method, the TD solutions are recovered by manipulating the FD spectral integrals into a form from which one may infer the TD solutions. In the STT, on the other hand, the FD integrals are converted to the TD so that the TD fields are expressed as a spatial-spectrum integral of *transient plane waves*. This STT integral can be evaluated in a closed form, leading to results that are similar to those derived via the CdH method in those cases where the latter is applicable. Yet the STT provides a more flexible framework that may be used in cases where the CdH cannot be applied, e.g., problems involving reflections and diffraction of complex source pulsed beams (CSPB) [16, 17] (see STT solutions of 3D-CSPB reflection and diffraction at plane dielectric interfaces [18] and at wedges [19–21]). One of the main goals of the present paper is to discuss the concepts of the STT in the context of the AiPB where the CdH approach is not applicable.

The presentation starts in Section 2 with a wave-analysis of the AiB in the FD. It presents the ray interpretation of the AiB and the frequency scaling of the parameters such that the radiating field is *non-dispersive* in the sense that the ray skeleton and the propagation trajectory are frequency independent. The STT formulation and the derivation of the exact TD solution (21) are then considered in Section 3, following some numerical results that provide further insight into the wave mechanism of the AiB. The exact solution describes the field everywhere as an implicit function of space and time. One may derive explicit wavefront approximations for the time windows near the pulse arrival. This topic and others are discussed in [8].

2 Non dispersive Airy beams – frequency domain representation

The finite-energy non dispersive Airy beams (AiB) field $\hat{U}(x, z)$ in the half-space $z > 0$ of a 2D coordinate frame $\mathbf{r} = (x, z)$ is generated by the aperture field distribution at $z = 0$

$$\hat{U}_0(x'; \omega) = \text{Ai}(\beta^{-1/3} k^{2/3} x') e^{\alpha k x'} \quad (1)$$

where x' refers to points in the aperture, Ai is the Airy function, and the exponential window is added in order to render the energy of this distribution finite. Here and henceforth, an over hat denotes time-harmonic constituents with harmonic time-dependence $e^{-i\omega t}$, $k = \omega/c$ and a subscript 0 indicates values in the $z = 0$ plane.

In (1) we used a specific frequency scaling of the parameters such that β and α are frequency-independent parameters. This scaling, first introduced in [7] in contradistinction to previous suggestions (e.g., [22]), ensures that the radiating AiB is *non-dispersive* in the sense that it has a *frequency independent ray skeleton* (see (7)) thus ensuring that all frequency components propagate along the same ray trajectories and focus onto the same caustic which delineated the AiB propagation trajectory (see (3)). We note that the parameters β and α used here are related to the parameters x_0 and α_0 used in the AiB literature (e.g., [2]) via $x_0 = \beta^{1/3} k^{-2/3}$ and $\alpha_0 = (k\alpha)^{1/3}$.

The paraxial solution for the radiating AiB field due to the initial conditions in (1) is [2]

$$\begin{aligned} \hat{U}(\mathbf{r}; \omega) = & \text{Ai}[(k\beta)^{2/3} (x/\beta - (z/2\beta)^2 + i\alpha z/\beta)] \\ & \times e^{ik(z+xz/2\beta-z^3/12\beta^2+\alpha^2 z/2)} e^{k\alpha(x-z^2/\beta)}. \end{aligned} \quad (2)$$

One readily verifies that the beam envelope shifts transversely without change along a parabolic trajectory (see Fig. 1)

$$x/\beta = (z/2\beta)^2. \quad (3)$$

Note that this trajectory is frequency-independent because of the frequency scaling of the parameters in (1).

2.1 Ray representation

In order to facilitate ray analysis we use the asymptotic expression $\text{Ai}(\xi) \sim (-\pi^2\xi)^{-1/4} \sin[2/3(-\xi)^{3/2} + \pi/4]$ for $\xi \ll -1$ and decompose the aperture

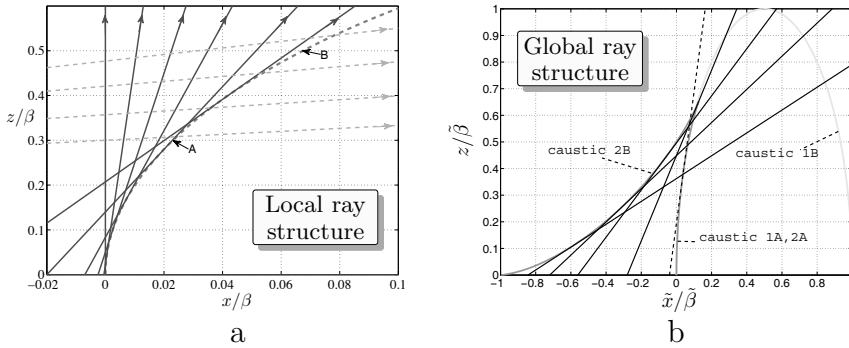


Figure 2: Local and global structures of ray species \hat{U}^+ . Note the scale difference of the x axes in (a) and (b). All axes are normalized. (a) The solid line rays radiate from the aperture at $z = 0$ and converge onto a caustic (dashed line). The dashed line rays originate at distant points where the aperture field is weak (see also (b)). They intersect the caustic at very late times, beyond the pertinent time-window of the AiPB, and do not focus there. These rays are not included in the paraxial solution of (2). Points $A = (x, z) = (0.023, 0.3)\beta$ and $B = (0.067, 0.5)\beta$ are typical points on the caustic where the field will be calculated in the sequel. (b) The global ray picture described by the cusped caustic formed by the two grey caustics 2A and 2B that merge into a cusp. This figure is taken from [7, Fig. 16]. That reference deals with 3D Airy beams, where the caustic has a much more complicated 3D structure of a *hyperbolic umbilic* catastrophe that evolves into a *parabolic umbilic* catastrophe [26, Fig. 7.3]. Nevertheless, since this figure depicts a cross sectional cut of the catastrophe in the symmetry plane, the cusped caustic above referred to describes also the ray structure of the 2D problem considered here with $\tilde{\beta} = \beta$ and $\tilde{x} = x$. It consists of two parts 2A and 2B that merge in a cusp. The solid lines are the corresponding rays.

field at $x \ll -k^{-2/3}\beta^{1/3}$ into a sum of two local plane wave constituents, viz.

$$\hat{U}_0(x') \approx A_0^+ \exp(ik\psi_0^+) + A_0^- \exp(ik\psi_0^-) \equiv \hat{U}_0^+(x') + \hat{U}_0^-(x') \quad (4)$$

where the initial phase and amplitude functions ψ_0^\pm and A_0^\pm are given by

$$k\psi_0^\pm(x') = \mp [k(2/3)(-x')^{3/2}\beta^{-1/2} + \pi/4] \quad (5)$$

$$A_0^\pm(x') = \pm(i/2\sqrt{\pi}) [-xk^{2/3}\beta^{-1/3}]^{-1/4} e^{\alpha kx'}. \quad (6)$$

We assume here that α is sufficiently small so that it is included in the amplitudes functions A_0^\pm and note in the phase ψ_0^\pm . This assumption will be removed in the exact TD analysis in Section 3.

The initial fields \hat{U}_0^\pm in (4) give rise to rays that emerge from points $x' < 0$ in the aperture at local angles (measured with respect to the z -axis)

$$\theta^\pm(x') = \sin^{-1} [\partial_{x'} \psi_0^\pm(x')] = \pm \sin^{-1} [(-x'/\beta)^{-1/2}]. \quad (7)$$

Ray species \hat{U}^- emerges to the left with respect to the z axis and diverges (dashed-dotted line rays in Fig. 1), giving rise to a weak contribution there. Ray species \hat{U}^+ emerges to the right (solid lines in Fig. 1) and converges to a caustic that delineates the curved beam trajectory. The paraxially approximated caustic is given in (3), but the exact caustic can be obtained via a standard ray analysis as outlined in the Appendix of [8].

From (7), the exit points x' of species $\hat{U}_0^+(x)$ corresponding to a given observation point $\mathbf{r} = (x, z)$ on the lit side of the caustic is found via

$$\sin \theta(x') = (-x'/\beta)^{-1/2} = (x - x')/\rho, \quad \rho = \sqrt{(x - x')^2 + z^2}, \quad (8)$$

with ρ denoting the distance along the ray. This equation has *three* solutions, denoted as $x'_{1,2,3}$ in accord with their arrival times. Rays 1 and 2 converge onto the caustic such that ray 2 has touched the caustic before reaching the observer while ray 1 has not (see Figs. 1 and 2(a)). The third solution corresponds to rays that originate at distant points where the aperture field is weak (dashed lines in Fig. 2(a)). They intersect the caustic at very late times, beyond the pertinent time-window of the AiPB, and yield weak contributions. By definition, these contributions are not included in the paraxial solution of (2). Note that the paraxially approximated caustic in (3) is obtained from (8) by replacing there $\rho \rightarrow z$.

The complete (exact) ray structure calculated via (8) is described by the cusped caustic in Fig. 2(a) consisting of two caustics 2A and 2B (grey lines) that merge in a cusp (Fig. 16 from [7]). Caustic 2A is formed by the convergence of rays 1 and 2, and describes the AiB propagation trajectory. Caustic 2B is formed by the convergence of rays 1 and 3, and, as noted earlier, it is irrelevant for the field near the AiB propagation trajectory. Note that beyond the cusp, the field disperses and loses its beam shape. This limits the AiB propagation range to a distance of order 0.6β (see Fig. 2(a)) hence β should be chosen according to application. The range is also determined by the parameter α which controls the decay rate along the beam axis.

The field of the AiB may now be calculated using ray techniques. A uniform ray-based solution that is valid near the caustic where the standard ray solution fails, has been derived in [6] via the the uniform geometrical optics (UGO) [23, 24]. The UGO solution fully agrees with the paraxially approximated AiB solution in (2) in the region where the latter is valid. This ray solution provides a cogent physical description to the AiB and explains

its intriguing properties. It is also more accurate than the solution in (2), in particular at large ranges where (2) fails since the parabolic trajectory in (3) deviates substantially from the true caustic obtained via the ray analysis. We do not present the analysis here; this has been done in [7] in the context of the more complicated 3D AiB (see Figs. 11,12 there).

3 Time domain solutions – Airy pulsed beams

As discussed in Section 2, the specific scaling of the initial field in (1) ensures that all frequency components of the field are AiB that propagate along the same curved trajectory (3). If the initial conditions are pulsed, they generate a non-dispersive wavepacket that propagates along the curved trajectory, henceforth denoted as Airy Pulsed Beams (AiPB).

The TD expression for the AiPB can be obtained by converting the FD paraxial solution (2). Here, however, we use an alternative approach which is based on an exact spectral representation in the TD via the spectral theory of transients (STT) [9–12]. This approach leads to an exact closed-form TD solutions for the AiPB and it does not suffer from the difficulties of the paraxial approximation noted above.

The following section reviews the concepts of the STT in the context of the AiPB. In Section 3.2 we construct the STT integral representation of the time-dependent AiPB field, which is a spatial-spectrum integral of *transient plane waves*. The general procedure for evaluating this integral is discussed in Section 3.3, while Section 3.4 presents the details of the spectral evaluation in the present case. Finally in Section 3.5 we present numerical results for the AiPB that provide new insight into the wave mechanism of the AiB.

3.1 Analytic signal formulation

Analytic signals are extensions of physical time signals that can accommodate a complex time variable. Therefore, they are a useful tool in TD wave theory in applications involving complex propagation times delays, e.g., in complex-spectrum representations such as the STT, or in accommodating the off-axis field of beams [16, 17].

An analytic TD wave-function is related to the FD solution $\hat{U}(\mathbf{r}; \omega)$ via the one sided Fourier transform

$$\hat{u}^+(\mathbf{r}, t) = \frac{1}{\pi} \int_0^\infty d\omega e^{-i\omega t} \hat{f}(\omega) \hat{U}(\mathbf{r}; \omega), \quad \text{Im}(t) \leq 0 \quad (9)$$

where \hat{U} is a frequency domain solution and $\hat{f}(\omega)$ is an arbitrary temporal spectrum. Since the integral converges for real t , it also converges for all $t \in \mathbb{C}^-$, the lower half of the complex plane, thus defining an analytic function there. Here and henceforth analytic signals are denoted by an over + symbol. The physical signal field for real t is obtained by

$$u(\mathbf{r}, t) = \text{Re} \left[\overset{+}{u}(\mathbf{r}, t) \right], \quad \text{Im}(t) \uparrow 0. \quad (10)$$

Actually, multiplying $\overset{+}{u}$ by a complex parameter $e^{i\gamma}$, $\gamma \in [-\pi, \pi]$, one obtains via (10) a real solution $u(\mathbf{r}, t)$ as a linear combination of $\text{Re} \left(\overset{+}{u} \right)$ and $\text{Im} \left(\overset{+}{u} \right)$.

In (15) we make use of the convolution theorem for analytic signals. Stated generally, given two analytic signals $\overset{+}{f}$ and $\overset{+}{g}$, with spectra \hat{f} and \hat{g} , the analytic signal $\overset{+}{w}$ corresponding to $\hat{w} = \hat{f}\hat{g}$ is

$$\begin{aligned} \overset{+}{w}(t) &= \frac{1}{\pi} \int_0^\infty d\omega e^{-i\omega t} \hat{f}(\omega) \hat{g}(\omega) = \frac{1}{2} \int_{-\infty}^\infty dt' \overset{+}{f}(t') \overset{+}{g}(t-t') \\ &\equiv \frac{1}{2} \overset{+}{f}(t) \otimes \overset{+}{g}(t), \end{aligned} \quad (11)$$

where $\text{Im}(t) \leq 0$ while the t' -integration is performed along the real axis.

3.2 STT integral representation of the AiPB

In order to derive the STT representation of the AiPB, namely its representation as a spectrum of *transient plane-waves*, we start with the spectral (plane-wave) representation of the FD aperture field (1) [25, Eq. (9.5.4)]

$$\hat{U}_0(x'; \omega) = \frac{\omega^{1/3}}{2\pi} \int_{-\infty}^\infty d\xi A e^{i\omega\tau_0(\xi)} e^{i\omega\xi x'/c}, \quad (12)$$

$$\tau_0(\xi) = \beta(\xi + i\alpha)^3/3c, \quad A = (\beta/c)^{1/3} \quad (13)$$

where $e^{i\omega\xi x'/c}$ in (12) is identified as the Fourier kernel, and the spectral variable ξ is normalized such that the frequency ω appears explicitly in this kernel. With this normalization, ξ has a *frequency-independent* geometrical interpretation that enables a closed form inversion of the spectrum to the TD, as in (15).

The radiated field is obtained by adding the spectral propagator, viz.

$$\hat{U}(\mathbf{r}; \omega) = \frac{\omega^{1/3}}{2\pi} \int_c d\xi A e^{i\omega\tau(\xi)}, \quad \tau(\xi; \mathbf{r}) = \tau_0(\xi) + \xi x/c + \zeta z/c \quad (14)$$

where $\zeta = \sqrt{1 - \xi^2}$ is the spectral wave-number in the z -direction, chosen with $\text{Im}(\zeta) \geq 0$ for $\omega > 0$, and the integration contour \mathcal{C} extends along the real ξ axis from $-\infty$ to ∞ , passing above and below the branch point $\xi = \mp 1$ corresponding to ζ (Fig. 3). Equation (14) expresses the field as a spectrum of plane-waves propagating at angles $\theta(\xi) = \sin^{-1} \xi$ with respect to the z axis.

The TD solution is obtained now by applying the analytic (one-sided) Fourier transform (9), obtaining

$$\overset{+}{u}(\mathbf{r}, t) = \frac{1}{2\pi^2} \int_0^\infty d\omega e^{-i\omega t} \hat{g}(\omega) \int_{\mathcal{C}} d\xi A e^{i\omega\tau(\xi)} \quad (15)$$

where, for simplicity, we use $\hat{f}(\omega) = \omega^{-1/3} \hat{g}(\omega)$.

The reasons for using the analytic signal formulation are:

- The non dispersive spectral integral in (14) has a different form for $\omega > 0$ and $\omega < 0$ (e.g., for $\omega < 0$, the square root of ζ in (14) should be chosen with $\text{Im}(\zeta) \leq 0$). Leaving out the negative frequencies simplifies the analysis.
- The one sided transform allows using $\text{Im}(t) \leq 0$ and switching the order of the ξ and ω integrations in (15). The latter can then be evaluated in closed-form as in (16).
- Adding a small imaginary part to t displaces the location of the integrand's singularities in the complex ξ plane in a way that clarifies their location with respect to the integration path (see (19)).

Following the discussion above, we switch the order of integrations in (15) and evaluate the ω integration in a closed form, using also (11), obtaining

$$\overset{+}{u}(\mathbf{r}, t) = \frac{1}{2} \overset{+}{g}(t) \otimes \frac{-i}{2\pi^2} \int_{\mathcal{C}} d\xi \frac{A}{t - \tau(\xi)}. \quad (16)$$

The ξ -integral in (16), denoted as the *STT integral*, represents the field as a spectrum of transient plane-waves. It is convenient at this point to change the definition of the complex square root in ζ such that $\text{Re}(\zeta) \geq 0$ on the upper Riemann sheet [9, 10]. The resulting branch cuts of ζ extend along the real ξ -axis from ∓ 1 to $\mp \infty$, respectively (Fig. 3). This change has no effect on the result of the integral.

There are several classes of signals for which the convolution above can be evaluated in a closed-form. Here we use the class of analytic δ signals whose spectral and temporal counterparts are given by

$$\hat{g}(\omega) = e^{i\gamma} (-i\omega)^m e^{-\omega T}, \quad \overset{+}{g}(t) = e^{i\gamma} \overset{+}{\delta}^{(m)}(t - iT) = e^{i\gamma} \partial_t^m \frac{1}{\pi i} \frac{1}{t - iT} \quad (17)$$

with $m = 0, 1, 2, \dots$. The parameter $T > 0$ is proportional to the pulse length. The amplitude parameter $e^{i\gamma}$, where $\gamma \in [-\pi, \pi]$, controls the balance between the real and imaginary parts of the analytic signal when one calculates the physical signal via (10). The function $\overset{+}{\delta}^{(m)}$ is the m -th derivative of the analytic δ function, having m oscillations for $|t| < T$ and a t^{-m-1} decay rate for $|t| \gg T$. In the example of Section 3.5 we use $m = 2$.

Using (17) and (11), Eq. (16) becomes

$$\overset{+}{u}(\mathbf{r}, t) = \partial_t^m \frac{-ie^{i\gamma}}{2\pi^2} \int_C d\xi \frac{A}{t - \tau(\xi) - iT}. \quad (18)$$

3.3 Evaluation of the STT integral

The integral in (18) has time-dependent poles $\xi(t)$ in the complex ξ plane, defined by

$$\tau[\xi(t)] = \beta(\xi + i\alpha)^3/3c + \xi x/c + \zeta z/c = t - iT. \quad (19)$$

The solutions $\xi(t)$ to (19) are generally found numerically via a search algorithm. This search is simplified by using, as a starting point, the paraxial approximation $\zeta \approx 1 - \xi^2/2$, in which case (19) reduces to a third order polynomial equation with a closed-form solution. These solutions are generally complex, and are located in the upper and in the lower Riemann sheets (URS or LRS, respectively), where $\text{Re}(\zeta) \geq 0$. Further details are given in Section 3.4 and Figs. 3 and 4.

The integral in (18) can be evaluated by closing the integration contour at infinity about the lower or the upper half of the complex ξ -plane, thus expressing the field as contributions from the poles $\xi(t)$ lying in the respective half plane, plus a contribution from the branch-cuts of ζ that extend along the real ξ -axis,

$$\overset{+}{u}(\mathbf{r}, t) = \mp \sum_p \partial_t^m \frac{A e^{i\gamma}}{\pi \tau'[\xi^{(p)}(t)]} + \partial_t^m \frac{-ie^{i\gamma}}{2\pi^2} \int_{\mathcal{I}_b^\pm} d\xi \frac{A}{t - \tau(\xi) - iT} \quad (20)$$

$$\simeq \mp \sum_p \partial_t^m \frac{A e^{i\gamma}}{\pi \tau'[\xi^{(p)}(t)]} \quad (21)$$

where the upper and lower signs correspond to the upper or lower half-plane closures, respectively. The first term in (20) represents the contribution of all the poles $\xi^{(p)}(t)$ in the respective half plane with p being an index and $\tau' = \partial_\xi \tau$. Referring, for example, to the ξ -plan configuration in Figs. 3 and 4 (see discussion in Section 3.4 below), choosing the upper or the lower

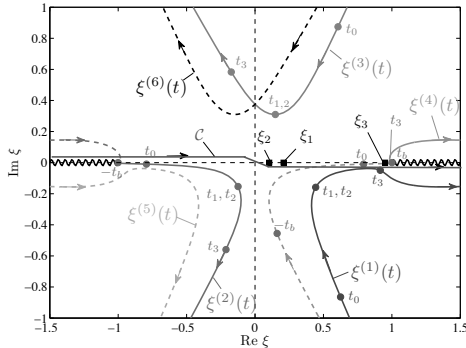


Figure 3: The complex ξ plane of the STT integral (18) for a typical observation point on the lit side of caustic (specifically, this point is displaced horizontally by $\Delta_x = -2.5 \cdot 10^{-3} \beta$ from point A in Fig. 2(a) that resides on the caustic). Wiggly lines: branch cuts of ζ separating the upper Riemann sheet (URS) where $\text{Re } \zeta > 0$ from the lower Riemann sheet (LRS) where $\text{Re } \zeta < 0$. \mathcal{C} : the integration contour in Eqs. (14) and (18). Square tags: stationary points $\xi_{1,2,3}$ corresponding to rays $r = 1, 2, 3$ in Fig. 1 (for clarity, ray 3 is suppressed in Fig. 1 but it is shown in Fig. 2(a)). $t_{1,2,3}$: ray arrival times. Note that $t_1 \sim t_1$, but $t_3 - t_{1,2} \gg T$. $\xi^{(p)}(t)$, $p = 1, 2, \dots, 6$: trajectories of the 6 poles $\xi(t)$ of (19) as a function of t ; poles on the URS and LRS are denoted by solid or dashed lines, respectively. The tags on the trajectories denote values of t there. The poles $p = 1, 3$ are always in the URS; $p = 5, 6$ are always in the LRS; $p = 2, 4$ are located first in the LRS and then cross to the URS. In order to improve visibility, we displaced the poles from the real ξ axis by choosing large T , $T = 10^{-2} \beta/c$, but in the field calculations we used $T = 10^{-6} \beta/c$, yielding the poles map in Fig. 4. Here and in the following figures we used $\alpha = 10^{-5}$.

half plane closure implies that the summation involves the pole $p = 3$ or the poles $p = 1, 2$, respectively. The second term in (20) is the contribution of the branch-cuts \mathcal{I}_b^\pm of ζ extending, respectively, along the real ξ -axis segments $\xi \in [1, \infty)$ and $\xi \in (-\infty, -1]$ (wiggly lines in Fig. 3). In (21), the branch-cut integrals have been neglected since they correspond to the evanescent spectrum. Finally, we note that ∂_t can be calculated in a closed-form by noting from (19) that $\partial_t \xi(t) = \{\tau'[\xi(t)]\}^{-1}$.

The result in (21) expresses the field everywhere as an implicit function of space and time. As noted in the Introduction, wavefront approximations near the rays arrival times, expressed explicitly in terms of the space-time coordinates, have been derived in [8].

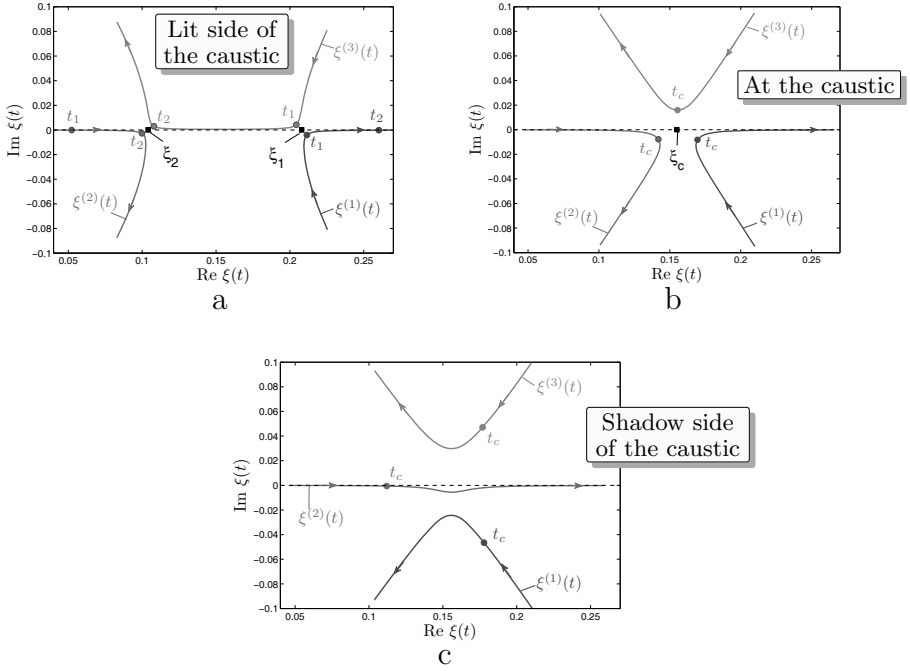


Figure 4: Trajectories of the poles $\xi^{(p)}(t)$, $p = 1, 2, 3$ of (19) in the complex ξ plane for observation points near point A of Fig. 2(a) that resides on the caustic. The figure zooms on the spectral zone near the stationary points $\xi_{1,2}$ of Fig. 3 (square tags) and the trajectories are marked by the same numbers and tags as in Fig. 3. Pulse length parameter: $cT/\beta = 10^{-6}$. (a) Observation point on the lit side of the caustic; (b) on the caustic; (c) on the shadow side. Specifically in this figure, the point in (a) is displaced horizontally from A by $\Delta_x = -2.5 \cdot 10^{-3}\beta$ and the point in (c) is displaced by $\Delta_x = 2.3 \cdot 10^{-4}\beta$. On the caustic, the two stationary points coalesce to a 2nd order stationary point ξ_c and both rays $r = 1, 2$ arrive at $t = t_c$.

3.4 Spectral properties of the STT integral

We start with the properties of $\tau(\xi)$, referring to Fig. 3 which depicts the ξ -plane for a given \mathbf{r} on the lit side of the caustic (specifically, near point A of Fig. 2(a) that resides on the caustic). $\tau(\xi)$ has three stationary points, denoted by ξ_r , $r = 1, 2, 3$, shown in Fig. 3 as square tags. $\xi_1 = 0.208$ and $\xi_2 = 0.104$ correspond to rays 1 and 2 in Fig. 1, where ray 1 has not touched the caustic yet while ray 2 has touched it. The aperture exit points of these rays are $x'_1 = -0.043\beta$ and $x'_2 = -0.011\beta$ and the arrival times are $t_1 = 0.3007\beta/c$ and $t_2 = 0.3009\beta/c$.

The stationary point $\xi_3 = 0.951$ corresponds to a ray that emerges from a

very remote point $x'_3 = -0.9\beta$ in the aperture and propagates almost parallel to the aperture ($\xi_3 \lesssim 1$), reaching \mathbf{r} at a later time $t_3 = 0.39\beta/c$ (note that $t_1 \approx t_2$ but $t_3 - t_{1,2} \approx 0.09\beta/c \gg T$ where T is typically $\sim 10^{-6}\beta/c$). For clarity, this ray is suppressed in Fig. 1 but it is shown in Fig. 2 where one may see that, unlike rays 1 and 2, it *intersects* the caustic and does not *converge onto it*. It also has a relatively weak contribution due to the $e^{k\alpha x'}$ decay in the aperture (see (1)). This ray is not included in the paraxial approximation (2).

Equation (19) has 6 roots $\xi^{(p)}(t)$, $p = 1, \dots, 6$, at any given t . Figure 3 depicts their trajectories in the complex ξ -plane as a function of t at the point A referred above. The poles may be located either on the URS or the LRS where they are denoted by solid or dashed trajectories, respectively. The tags on the trajectories indicate the corresponding values of t . The poles $p = 1, 3$ are located always on the URS, while $p = 5, 6$ are always on the LRS. At a very early time, the poles $p = 2, 4$ are located in the LRS and then cross to the URS at $t = \mp t_b$, $t_b > 0$, respectively, never crossing to the LRS again. Note that the trajectories in Fig. 3 are calculated for a wide pulse with $cT = 10^{-2}\beta$ in order to displace the poles from the real ξ axis and to clarify their location with respect to the integration contour \mathcal{C} . In practice, however, T is much smaller: in Fig. 4 and henceforth we use $cT = 10^{-6}\beta$.

For $t \approx t_{1,2}$ near the pulse arrival time, the poles $p = 1, 2, 3$ converge to the stationary points $\xi_{1,2}$ in the URS. Figure 4 zooms in on this spectral zone for three observation points: on the lit side of the caustic, on the caustic, and in the shadow side. Each case is characterized by a different arrangement of the stationary points and of the poles, as follows from the different spectral properties of $\tau(\xi)$. One should note though that the overall poles-topology is similar in all three cases, with poles $p = 1, 2$ being in the lower half of the URS with respect to \mathcal{C} , while pole $p = 3$ is in the upper half of the URS. Thus, the field in (21) is described by the two poles $p = 1, 2$ if one chooses a lower half plane closure, or by a single pole $p = 3$ if one chooses an upper half plane closure. We also note that at a later time $t = t_b$, the pole $p = 4$ crosses the branch cut and enters the URS near ξ_3 , never crossing to the LRS again. However, as mentioned earlier, this contribution is weak and it is beyond the pertinent time window.

3.5 The AiPB field

In view of the discussion in the preceding paragraph, we have calculate the field by using an upper half plane closure in (21) so that the field is given

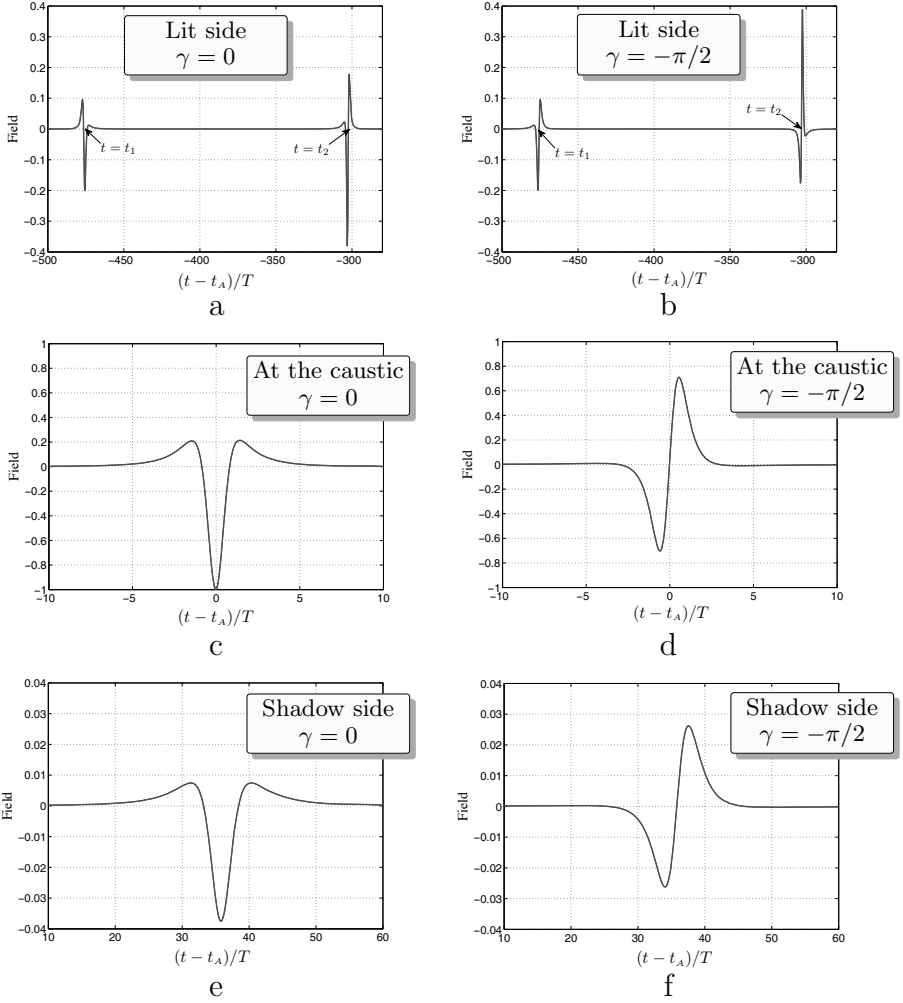


Figure 5: The waveforms near the caustic: (a,b), (c,d) and (e,f) correspond to points on the lit side of the caustic, on the caustic at point A, and on the shadow side, respectively. They are calculated exactly via (21). The temporal signal is (17) with $m = 2$ and $\gamma = 0$ in (a,c,e) or $\gamma = -\pi/2$ in (b,d,f). Note that the waveforms for $\gamma = -\pi/2$ are Hilbert transforms of those for $\gamma = 0$. The time axis is centered around t_A , the arrival time to A, and normalized with respect to T . The field is normalized such that $\max |u| = 1$ on the caustic in (c). Note also the different vertical scales.

by the single pole $p = 3$ in Figs. 3 and 4, viz.

$$\dagger \dot{u}(\mathbf{r}, t) = -\partial_t^m \frac{A e^{i\gamma}}{\pi \tau' [\xi^{(3)}(t)]}. \quad (22)$$

Figure 5 depicts the field at the 3 observation points considered in Fig. 4, located near point A in Fig. 2. The temporal signal is given by (17) with $m = 2$ and $\gamma = 0$ in (a,c,e) or $\gamma = -\pi/2$ in (b,d,f). The field is calculated exactly via the real part of (22) (the case $\gamma = -\pi/2$ is the same as taking the imaginary part of (22) for $\gamma = 0$, and it is a Hilbert transform of the case $\gamma = 0$).

On the lit side of the caustic (Figs. 5(a,b)) there are two separate peaks at $t_{1,2}$, which are obtained when this pole passes near the stationary points $\xi_{1,2}$ where τ' vanishes so that $\tau'[\xi^{(3)}(t)]$ in the denominator of (22) is small. On the caustic (Figs. 5(c,d)), these two peaks coalesce to a stronger peak, obtained when the pole passes near the second order stationary point ξ_c in Fig. 4(b). Finally, on the shadow side of the caustic (Figs. 5(e,f)), the pulse evanesces, as follows also from the fact that the pole $p = 3$ in Fig. 4(c) passes far away from the real ξ axis.

Figure 6 depicts snapshots of the field in the vicinity of points A and B on the caustic, defined in Fig. 2(a). The snapshots are taken at the arrival times at each point. The field on the lit side consists of wavefronts 1 and 2 corresponding to ray species $r = 1$ that converges toward the caustic and ray species $r = 2$ that diverges away from it. Species $r = 1$ originate from points x' in the aperture that are further away from its center and therefore arrive at larger angles with respect to the z -axis. The two species coalesce on

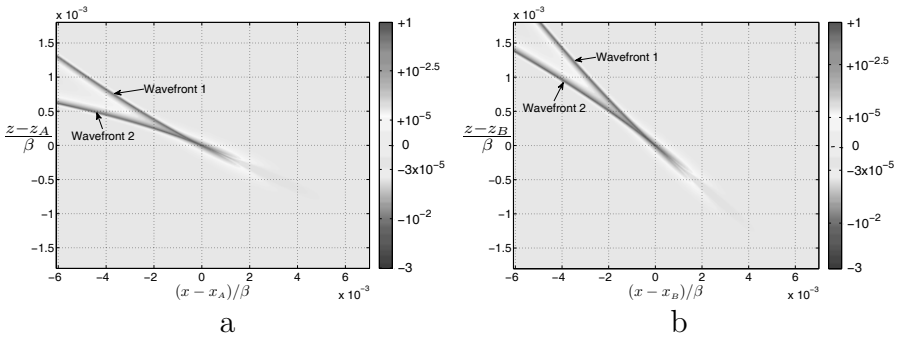


Figure 6: Snapshots of the field near points A (a) and B (b) on the caustic. The snapshots are taken at $t = t_{A,B}$ denoting the time of arrival at A and B, respectively. The axes are centered around point A and B and are normalized with respect to β . The temporal signal is given by (17) with $m = 2$, $\gamma = 0$, $T = 10^{-6}\beta/c$ and $\alpha = 10^{-5}$. The logarithmic scale retains the sign of the waveform (see the bar), and is normalized with respect to the maximal value in (a). ‘Wavefronts 1,2’ corresponding to rays species $r = 1,2$, respectively, coalesce at the caustic with an evanescent contributions on the shadow side.

the caustic generating the strong peak of the beam that follows the curved trajectory. The field on the shadow side decays algebraically, as opposed to the exponential decay in the time-harmonic case. Note also the wavefront rotation as the pulse progresses along the caustic from point A to B, which is due to the bending of the caustic and the fact that rays reaching the caustic at longer ranges arrive at increasingly sharper angles (see Fig. 1).

The resolution of Fig. 6 fails to depict the narrow negative peak of the wavefronts (see Fig. 5). We therefore depict in Figs. 7 cross sectional cuts of the snapshot in Fig. 6(a). The cut in Fig. 7(a) passes exactly through point A, demonstrating the strong peak at the caustic, as opposed to the peaks of the rays in Fig. 7(b).

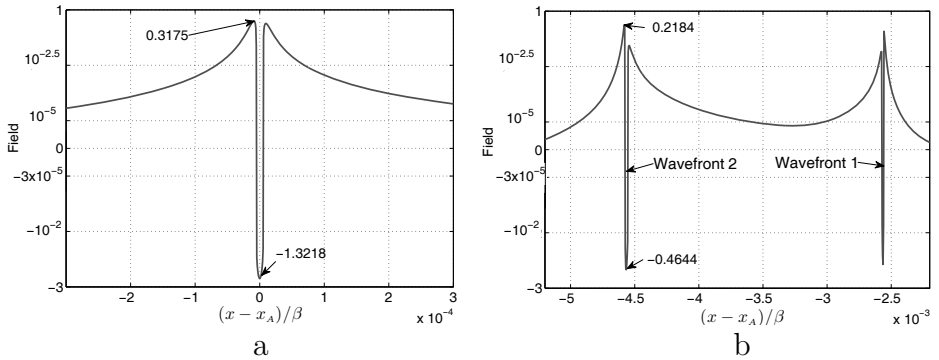


Figure 7: Cross sectional cuts along $z = \text{constant}$ lines in Fig. 6(a). (a) Cut passing exactly through A ($z - z_A = 0$); (b) cut along $z - z_A = 0.5 \cdot 10^{-3} \beta$.

Figure 8 explores the effect of the parameter α that controls the exponential decay of the aperture field (see (1)). Increasing α affects essentially the $r = 1$ ray species that arrives first, since this species originates from aperture points x' that are located further away from the center and are therefore strongly affected by the exponential decay. Indeed, comparing Figs. 8(a,b) with Figs. 6(a,b) one observes that the field of ‘wavefront 1’ is weaker and has a longer pulse length. For the same reason, the field becomes weaker as it propagates further away from point A to B.

4 Conclusions

In this paper we discussed the Airy Beams (AiB) and the ultra wide band (UWB) Airy Pulsed Beams (AiPB). We discussed the physical properties of these wave functions and the mathematical techniques that are involved in calculating the solutions in the frequency domain (FD) and in the time domain (TD).

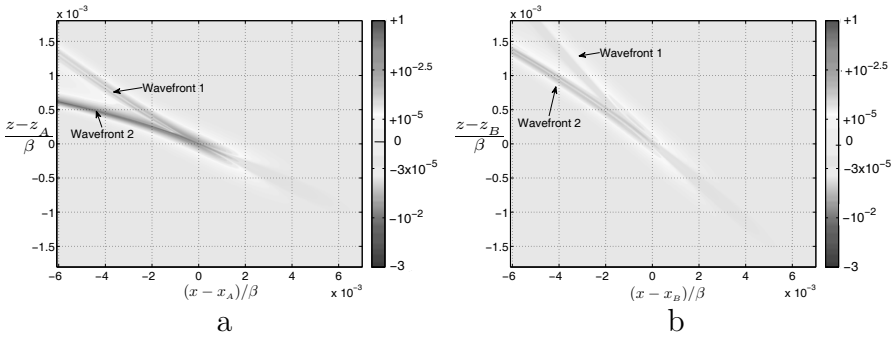


Figure 8: Snapshots of the field near points A (a) and B (b) on the caustic. All parameters are the same as in Fig. 6, except for $\alpha = 10^{-3}$.

We started in Section 2.1 with a ray analysis of the FD solution. The ray representation provides a cogent physical interpretation to the AiB and explains its intriguing properties. The ray formulation, when applied judiciously, is more accurate than the paraxial solution of (2), mainly due to the growing deviation of the paraxial propagation trajectory (3) from the exact trajectory obtained via ray analysis. In particular, the paraxial theory does not predict the cusp in Fig. 2(b) beyond which the AiB disperses. The error of the paraxial solution versus the exact ray solution is studied in [7, Figs. 11 and 12] in the context of the 3D AiB. Note that the error is obtained even at a relatively short range $z \sim 0.16\beta$.

The formulation of the UWB-AiPB solution is based on a frequency scaling of the initial aperture field in (1). This scaling, first introduced in [8], renders the FD AiB solution *non-dispersive* in the sense that the ray skeleton of the field is frequency independent. This ensures that all the frequency components are AiB's that propagate along the same curved trajectory, so that the TD wavepacket does not disperse due to the wide frequency band.

An exact closed-form solution to the AiPB has been derived in Section 3 via the spectral theory of transients (STT). The STT synthesizes the field as a spectral integral of time dependent plane waves. This integral is then evaluated in a closed form and the final result in Eq. (21) expresses the field compactly by tracking the time-dependent spectral poles of the integrand. Actually, the AiPB is expressed in (21) by the contribution of a single pole.

The properties of the AiPB were explored in Section 3.5 via a detailed numerical example. It has been shown that the AiPB indeed propagates along a curved caustic while retaining its field structure. From Fig. 6 one concludes that the AiPB consists of two propagating wavefronts that coalesce

on the caustic, generating a strong peak there. The wave mechanism of the AiPB is explained further in Fig. 8 where one may discern that the first arriving wavefront is weaker than the second one. This is due to the fact that this waveform is formed by rays originating from more distant points at the aperture that are affected more strongly by the attenuation parameter α . This demonstrates again that the AiB is, in fact, not a beam field in the sense that it is not described by a local beam dynamics [6]. One also observes that the STT solution applies uniformly through the caustic, from the lit side to the shadow.

The emphasis in this paper has been placed on the exact spectral solution via the STT, which is an extension of the Cagniard–de Hoop (CdH) method. In the CdH approach, the TD solutions are obtained by manipulating the FD spectral integrals into a form from which one may infer the TD solutions ‘by inspection’. Specifically, in that approach the integration contour of the original FD spectral integral are deformed to a CdH contour which is defined by the solution of (19) (with $T \rightarrow 0$) with t being a parameter along the CdH contour that increases monotonically from some finite value, say t_0 , to infinity. From the solution of Eq. (19) as a function of t shown in Figs. 3 or 4 one readily observes that it is impossible to find a simple deformation of the original integration contour \mathcal{C} to a path whereon the parameter t increases monotonically as explained above. In the STT approach, this difficulty is circumvented by formulating the field as a TD spectral integral and then evaluating this integral by closing the integration contour \mathcal{C} about *all* the relevant singularities in the complex-spectrum plane. The present example demonstrates that the STT is indeed a flexible reformulation of the CdH method.

Acknowledgment

This work is supported in part by the Israeli Science Foundation, under Grant No. 263/11. EH would like to extend his warm thanks to Professor Adrianus T. de Hoop for inspiring discussions on the relation between the CdH method and the STT.

Bibliography

- [1] G. A. Siviloglou, J. Broky, A. Dogariu, and D. N. Christodoulides, “Observation of accelerating Airy beams,” *Phys. Rev. Lett.*, vol. 99, pp. 213901-1–213901-4, Nov. 2007.

-
- [2] G. A. Siviloglou and D. N. Christodoulides, “Accelerating finite energy Airy beams,” *Opt. Lett.*, vol. 32, no. 8, pp. 79–981, April 2007.
 - [3] M. A. Bandres and J. Gutiérrez-Vega, “Airy-Gauss beams and their transformation by paraxial optical systems,” *Opt. Express*, vol. 15, no. 25, pp. 16719–16728, Dec. 2007.
 - [4] G. A. Siviloglou, J. Broky, A. Dogariu, and D. N. Christodoulides, “Ballistic dynamics of Airy beams,” *Opt. Lett.*, vol. 33, no. 3, pp. 207–209, Feb. 2008.
 - [5] J. Broky, G. A. Siviloglou, A. Dogariu, and D. N. Christodoulides, “Self-healing properties of optical Airy beams,” *Optics Express*, vol. 16, no. 17, pp. 12880–12891, Aug. 2008.
 - [6] Y. Kaganovsky and E. Heyman, “Wave analysis of Airy beams,” *Optics Express*, vol. 18, no. 8, pp. 8440–8452, April 2010.
 - [7] Y. Kaganovsky and E. Heyman, “Non-paraxial wave analysis of 3D Airy beams,” *J. Opt. Soc. Am. A*, vol. 29, no. 5, pp. 671–688, May 2012.
 - [8] Y. Kaganovsky and E. Heyman, “Airy pulsed beams,” *J. Opt. Soc. Am. A*, vol. 28, no. 6, pp. 1243–1255, June 2011.
 - [9] E. Heyman and L. B. Felsen, “Weakly dispersive spectral theory of transients (STT), Part I: Formulation and interpretation,” *IEEE Trans. Antennas Propag.*, vol. 35, no. 1, pp. 80–86, Jan. 1987.
 - [10] E. Heyman and L. B. Felsen, “Weakly dispersive spectral theory of transients (STT), Part II: Evaluation of the spectral integral,” *IEEE Trans. Antennas Propag.*, vol. 35, no. 5, pp. 574–580, May 1987.
 - [11] E. Heyman, “Weakly dispersive spectral theory of transients (STT), Part III: Applications,” *IEEE Trans. Antennas Propag.*, vol. 35, no. 11, pp. 1258–1266, Nov. 1987.
 - [12] E. Heyman and L. B. Felsen, “Real and complex spectra – an alternative view of WKB seismograms,” *Geophys. J. Roy. Astro. Soc.*, vol. 91, no. 3, pp. 1087–1126, Dec. 1987.
 - [13] L. Cagniard, *Reflection and Refraction of Progressive Seismic Waves*, (Translation by E. Flinn, C. H. Dix, of *Réflexion et réfraction des ondes sismiques progressives*, Paris, Gauthier-Villars, 1939) New York: McGraw-Hill, 1962.
 - [14] A. T. de Hoop, “A modification of Cagniard’s method for solving seismic pulse problems,” *Appl. Sci. Res.*, Sect. B, no. 8, pp. 349–356, May 1960.
 - [15] A. T. de Hoop and H. J. Frankena, “Radiation of pulses generated by a vertical electric dipole above a plane, non-conducting, earth,” *Appl. Sci. Res.*, Sect. B, no. 8, pp. 369–377, May 1960.
 - [16] E. Heyman and L. B. Felsen, “Gaussian beam and pulsed beam dynamics: complex source and spectrum formulations within and beyond paraxial asymptotics,” *J. Opt. Soc. Am. A*, vol. 18, no. 7, pp. 1588–1610, July 2001.

- [17] E. Heyman, "Pulsed beam solutions for propagation and scattering problems," in *Scattering: Scattering and Inverse Scattering in Pure and Applied Science*, E. R. Pike and P. C. Sabatier (eds.), Academic Press, vol. 1, chap. 1.5.4, pp. 295–315, 2002.
- [18] E. Heyman, R. Strachievitz, and D. Koslof, "Pulsed beam reflection and transmission at a planar interface: Exact solutions and approximate local models," *Wave Motion*, vol. 18, no. 4, pp. 315–343, Dec. 1993.
- [19] R. Iancu and E. Heyman, "Pulsed field diffraction by a perfectly conducting wedge: A spectral theory of transient (STT) analysis," *IEEE Trans. Antennas Propag.*, vol. 42, no. 6, pp. 781–789, June 1994.
- [20] R. Iancu and E. Heyman, "Pulsed beam diffraction by a perfectly conducting wedge. Exact Solution," *IEEE Trans. Antennas Propag.*, vol. 42, no. 10, pp. 1377–1385, Oct. 1994.
- [21] E. Heyman and R. Iancu, "Pulsed beam diffraction by a perfectly conducting wedge. Local scattering models," *IEEE Trans. Antennas Propag.*, vol. 43, no. 5, pp. 519–528, May 1995.
- [22] P. Saari, "Laterally accelerating Airy pulses," *Optics Express*, vol. 16, no. 14, pp. 10303–10308, July 2008.
- [23] D. Ludwig, "Wave propagation near a smooth caustic," *Bull. Amer. Math. Soc.*, vol. 71, no. 5, pp. 776–779, May 1965.
- [24] Y. A. Kravtsov, "A modification of the geometrical optics method," *Izv. VUZ Radiofiz.*, Engl. transl., *Radiophys. Quantum Electron.*, vol. 7, pp. 664–673, 1964.
- [25] F. W. J. Olver, D. W. Lozier, R. F. Boisvert, and C. W. Clark, eds., *NIST Digital Library of Mathematical Functions*, <http://dlmf.nist.gov/>, 2010. Release of 1.0.5 of 2012-10-01.
- [26] J. Nye, *Natural Focusing and Fine Structure of Light: Caustics and Wave Dislocations* Philadelphia, PA: Institute of Physics Pub., 1999.